Biomedical Optics EXPRESS

Wide-field Raman imaging for bone detection in tissue

Asael Papour,[1,*] Jin Hee Kwak,[2] Zach Taylor,[3] Benjamin Wu,[3] Oscar Stafsudd,[1] and Warren Grundfest[3]

[1]*Quantum Electronics Laboratory, Department of Electrical Engineering, University of California Los Angeles, Los Angeles, California 90095, USA*

[2]*Section of Orthodontics, School of Dentistry, University of California Los Angeles, Los Angeles, California 90095, USA*

[3]*Department of Bioengineering University of California Los Angeles, Los Angeles, California 90095, USA*

[*]*papour@ucla.edu*

Abstract: Inappropriate bone growth in soft tissue can occur after trauma to a limb and can cause a disruption to the healing process. This is known as Heterotopic Ossification (HO) in which regions in the tissue start to mineralize and form microscopic bone-like structures. These structures continue to calcify and develop into large, non-functional bony masses that cause pain, limit limb movement, and expose the tissue to reoccurring infections; in the case of open wounds this can lead to amputation as a result of a failed wound. Both Magnetic Resonance Imaging (MRI) and X-ray imaging have poor sensitivity and specificity for the detection of HO, thus delaying therapy and leading to poor patient outcomes. We present a low-power, fast (1 frame per second) optical Raman imaging system with a large field of view (1 cm^2) that can differentiate bone tissue from soft tissue without spectroscopy, this in contrast to conventional Raman microscopy systems. This capability may allow for the development of instrumentation which permits bedside diagnosis of HO.

OCIS codes: (90.5860) Scattering, Raman; (170.3880) Medical and biological imaging; (170.6935) Tissue characterization.

References and links

1. T. Buchwald, K. Niciejewski, M. Kozielski, M. Szybowicz, M. Siatkowski, and H. Krauss, "Identifying compositional and structural changes in spongy and subchondral bone from the hip joints of patients with osteoarthritis using Raman spectroscopy," J. Biomed. Opt. **17**(1), 017007 (2012).
2. A. Hashimoto, L. Chiu, K. Sawada, T. Ikeuchi, K. Fujita, M. Takedachi, Y. Yamaguchi, S. Kawata, S. Murakami, and E. Tamiya, "In situ Raman imaging of osteoblastic mineralization," J. Raman Spectrosc. **45**(2), 157–161 (2014).
3. S. R. Goodyear, I. R. Gibson, J. M. S. Skakle, R. P. K. Wells, and R. M. Aspden, "A comparison of cortical and trabecular bone from C57 Black 6 mice using Raman spectroscopy," Bone **44**(5), 899–907 (2009).
4. N. J. Crane, E. Polfer, E. A. Elster, B. K. Potter, and J. A. Forsberg, "Raman spectroscopic analysis of combat-related heterotopic ossification development," Bone **57**(2), 335–342 (2013).
5. T. A. Davis, F. P. O'Brien, K. Anam, S. Grijalva, B. K. Potter, and E. A. Elster, "Heterotopic ossification in complex orthopaedic combat wounds: quantification and characterization of osteogenic precursor cell activity in traumatized muscle," J. Bone Joint Surg. Am. **93**(12), 1122–1131 (2011).
6. J. A. Forsberg and B. K. Potter, "Heterotopic ossification in wartime wounds," J. Surg. Orthop. Adv. **19**(1), 54–61 (2010).
7. B. K. Potter, J. A. Forsberg, T. A. Davis, K. N. Evans, J. S. Hawksworth, D. Tadaki, T. S. Brown, N. J. Crane, T. C. Burns, F. P. O'Brien, and E. A. Elster, "Heterotopic ossification following combat-related trauma," J. Bone Joint Surg. Am. **92**(Suppl 2), 74–89 (2010).
8. J. A. Forsberg, B. K. Potter, E. M. Polfer, S. D. Safford, and E. A. Elster, "Do inflammatory markers portend heterotopic ossification and wound failure in combat wounds?" Clin. Orthop. Relat. Res. **472**(9), 2845–2854 (2014).
9. J. R. Peterson, P. I. Okagbare, S. De La Rosa, K. E. Cilwa, J. E. Perosky, O. N. Eboda, A. Donneys, G. L. Su, S. R. Buchman, P. S. Cederna, S. C. Wang, K. M. Kozloff, M. D. Morris, and B. Levi, "Early detection of burn induced heterotopic ossification using transcutaneous Raman spectroscopy," Bone **54**(1), 28–34 (2013).

#239577 Received 22 Apr 2015; revised 19 Jun 2015; accepted 29 Jun 2015; published 10 Sep 2015

10. L. Nissim and D. Gilbertson-Dahdal, "An unusual complication of an infiltrated intravenous catheter: heterotopic ossification in a newborn," J. Radiol. Case Rep. **2**(2), 13–15 (2008).
11. B. P. Flannery, H. W. Deckman, W. G. Roberge, and K. L. D'Amico, "Three-dimensional X-ray microtomography," Science **237**(4821), 1439–1444 (1987).
12. M. G. M. Hunink and G. S. Gazelle, "CT screening: a trade-off of risks, benefits, and costs," J. Clin. Invest. **111**(11), 1612–1619 (2003).
13. M. V. Schulmerich, J. H. Cole, K. A. Dooley, M. D. Morris, J. M. Kreider, S. A. Goldstein, S. Srinivasan, and B. W. Pogue, "Noninvasive Raman tomographic imaging of canine bone tissue," J. Biomed. Opt. **13**(2), 020506 (2008).
14. J.-L. H. Demers, F. W. L. Esmonde-White, K. A. Esmonde-White, M. D. Morris, and B. W. Pogue, "Next-generation Raman tomography instrument for non-invasive in vivo bone imaging," Biomed. Opt. Express **6**(3), 793–806 (2015).
15. Y. Oshima, H. Sato, H. Kajiura-Kobayashi, T. Kimura, K. Naruse, and S. Nonaka, "Light sheet-excited spontaneous Raman imaging of a living fish by optical sectioning in a wide field Raman microscope," Opt. Express **20**(15), 16195 (2012).
16. H. R. Morris, C. C. Hoyt, P. Miller, and P. J. Treado, "Liquid Crystal Tunable Filter Raman Chemical Imaging," Appl. Spectrosc. **50**(6), 805–811 (1996).
17. J. Zhao, H. Lui, D. I. McLean, and H. Zeng, "Integrated real-time Raman system for clinical in vivo skin analysis," Skin Res. Technol. **14**(4), 484–492 (2008).
18. C. W. Freudiger, W. Min, B. G. Saar, S. Lu, G. R. Holtom, C. He, J. C. Tsai, J. X. Kang, and X. S. Xie, "Label-free biomedical imaging with high sensitivity by stimulated Raman scattering microscopy," Science **322**(5909), 1857–1861 (2008).
19. E. V. Efremov, J. B. Buijs, C. Gooijer, and F. Ariese, "Fluorescence rejection in resonance Raman spectroscopy using a picosecond-gated intensified charge-coupled device camera," Appl. Spectrosc. **61**(6), 571–578 (2007).
20. A. F. Palonpon, J. Ando, H. Yamakoshi, K. Dodo, M. Sodeoka, S. Kawata, and K. Fujita, "Raman and SERS microscopy for molecular imaging of live cells," Nat. Protoc. **8**(4), 677–692 (2013).

1. Introduction

Biocompatible Raman imaging of tissue, particularly imaging of tissue *in vivo*, has not yet translated to the clinical setting for several reasons. Most Raman techniques are time-consuming, require expensive and bulky systems, and are destructive in nature due to large illumination fluence [1–3]. There exist many disorders that cannot be detected or imaged via traditional methods and could use the high specificity that Raman signals offer. The detection of bone tissue that forms outside the skeleton hypothetically is an ideal candidate disorder, as the Phosphorus-Oxygen bond provides a strong unique Raman signature [1–4]. This mineralization growth occurs in traumatic wounds of the limbs where the injury affects soft tissue and is prevalent in combat wounds [5–8]. HO also arises in spinal injuries, severe burns and in the surgical beds resulting from orthopedic surgery complications [1,6,9,10]. The biochemical and physiologic mechanisms surrounding HO are not well understood and many precursors of HO are often poor predictors of the eventual establishment of HO, e.g. not all detectable fibrous abnormalities lead to HO [5,8]. In failed wounds in the extremities (limbs), bone growth is impossible to detect in the early stages and treatment includes resection of the ossified (mineralized) areas and topical or intravenous delivery of medications. The delayed detection followed by late treatment can lead to amputation to avoid potentially life threatening infection [4]. While early detection is crucial, current technologies including X-ray (CT) and Magnetic Resonance Imaging (MRI), are limited and do not offer the resolution and specificity that is required in HO detection. Typical resolution limit for a CT scan is about 1 mm [11] however these scans are not practical for daily patient monitoring due to high costs and, most importantly, high levels of ionizing radiation [12]. There is a clinical need for imaging techniques capable of providing fast, inexpensive, *in vivo* detection at a stage early enough to allow for appropriate treatment. Several research efforts employ multi-point tomographic imaging schemes for bone detection [13,14], while others use wide-field illumination and acquisition methods [15,16], yet no commercial imaging devices are currently available in the clinical setting. Traditional Raman systems involve point measurement and acquisition of Raman spectra using a spectrometer. The spectra obtained from such an acquisition procedure are then compared to a known spectral database to find a match. These spectra can serve as a fingerprint to identify elements of a sample and, in the

#239577 Received 22 Apr 2015; revised 19 Jun 2015; accepted 29 Jun 2015; published 10 Sep 2015

case of medical diagnostics, the constituents of tissue. In spectrometer based methodologies, detection is performed by raster scanning the sample area point by point and then coloring techniques are used to create contrast maps corresponding to the spatial location of particular constituents. This method is very specific; however, it is a time-consuming process that cannot be easily applied *in vivo* [17,18]. Two prominent problems are artifacts caused by the natural movements of the patients, and high fluence levels of the illumination source. Moreover, this methodology does not scale efficiently into imaging a large field of view of 0.1 cm^2 and above. Since stokes-Raman scattering exhibits low signal levels due to small cross section, a powerful laser source or alternately a focused beam is required in order to generate a detectable signal. High fluence levels can cause dehydration of the tissue, denaturation of proteins, and destruction of other constituents and is limited in *in vivo* tissue imaging by the Maximum Permissible Exposure (MPE) set by ANSI safety code [Z136.1-2007]. Broad fluorescence emission impose another difficulty in recording Raman signals and often requires photo-bleaching or extremely complicated laser systems to generate a 'cleaner' Raman signal [19]. Stokes Raman signals are several orders of magnitude weaker than fluorescence signals and several methods have been developed to amplify Raman signals, amongst them are stimulated themes such as Coherent Anti-stokes Raman Scattering (CARS) and Stimulated Raman Scattering (SRS) [20]. Clinical acceptance of these methods has not been proven due to the need for establishing a coherent illumination condition and the requirement of expensive and bulky laser systems. These patient sampling and biocompatibility issues indicate that traditional Raman techniques, though of extreme utility for *in vitro* or *ex vivo* settings, are currently not practical for *in vivo* or translational research applications.

2. Methods

The system was built around an 852 nm tunable narrow-band optical filter (Semrock, LL01-852-25) with 3 nm bandwidth (full-width half-maximum) mounted in front of the imaging optics and serves as the Raman band differentiator (Fig. 1). The tested imaging sensors were: Intensified CCD (ICCD) camera (Andor, iStar 334T) and Near Infra-Red (NIR) CCD camera (Andor, iKon-M 934). Both cameras were equipped with a 1 mega-pixel CCD sensor and provide 1 cm field of view, attained by a wide aperture macro lens (Canon, MP-E 65 mm). Diode laser illumination (Thorlabs, L785P090) supplies 90 mW power at 785 nm with ~1.4 nm bandwidth. Additional optical filters were encased in the detection optics platform to block light that falls outside the detection band: 785 nm notch filter (Semrock, NF03-785E-25), and a bandpass filter at 842 nm (Semrock, FF01-842/56-25) central wavelength with 30 nm spectral bandwidth (full-width half-maximum). The laser beam was defocused using an aspheric lens (Thorlabs, C280TME-B) and offered an illumination area of 30 mm^2 at a power density of 250 mW/cm^2, well below the MPE. The narrow band optical filter enables sensitive selection of the incoming signal from 849 to 852 nm. Tuning the narrow-band filter is done by changing the angle in which it is positioned in relation to the optical axis. Through angular adjustment, a multi spectral selection is achieved for each recorded image: 852 nm central wavelength at 0 degrees, to 849 nm at 10 degrees rotation. A pivot filter holder (Thorlabs, CP360R) was customized and coupled to a translation stage assembly for accurate rotation control. Rotation parameters of the filter were set upon calibration using a broad-band NIR LED source and a spectrometer (Ocean Optics, HR4000CG-UV-NIR). The final Raman map is computed by subtraction of two images (Fig. 2): First image captures the unique Raman stokes signal of the phosphate symmetric stretch at 960 cm^{-1}, and the second image captures only fluorescence and background signals of the tissue at 1002 cm^{-1}.

#239577 Received 22 Apr 2015; revised 19 Jun 2015; accepted 29 Jun 2015; published 10 Sep 2015

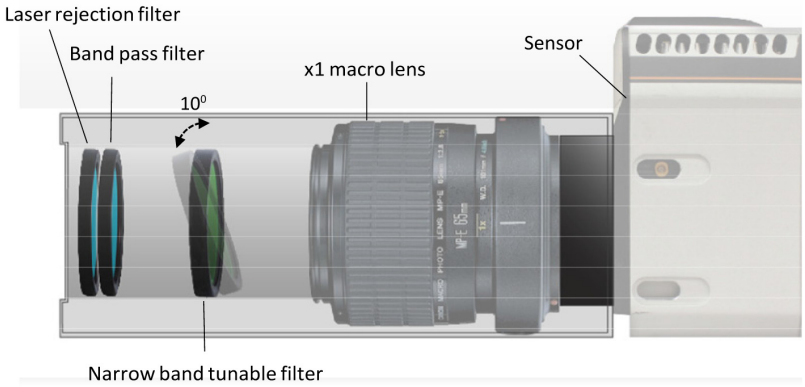

Fig. 1. Imaging system schematics: Intensified CCD camera sensor records 1 cm field of view images of a single wavelength band through set of optical filters. The tunable Raman filter in the heart of the system transmits 849 nm emission at 10 degrees pivot rotation and 852 nm emission at 0 degrees – perpendicular to the optical axes. Front filters include 785 nm laser rejection filter and a band pass filter reducing broad fluorescence signals. This compact imaging setup utilizes off the shelf parts: Macro lens, optical filters and a near infra-red sensor.

The Raman peak bandwidth is proportional to the laser linewidth and exhibits ~1.6 nm emission bandwidth. Although the tunable filter has broader transmission spectra than the Raman peak, good differentiation between muscle and bone is achieved due to lower muscle and bone fluorescence signals, compared with the high intensity bone peak. Further improvement in bone mapping and sensitivity can be achieved by utilizing a 2 nm bandwidth detection window.

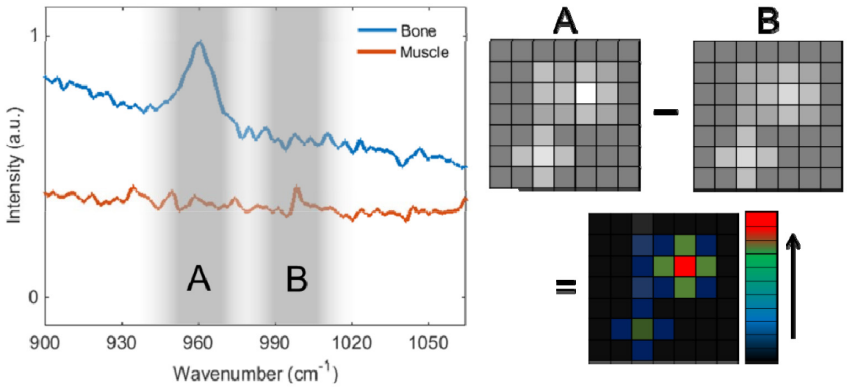

Fig. 2. Fluorescence and Raman spectrum of cortical bone and muscle tissues (left) with two imaging bands; A and B. Bone spectra shows the unique Raman signature of the phosphate at 960 cm^{-1} (Raman shift). Bone and muscle spectrum intensities realigned for better visualization. Image subtraction (right) removes the broad fluorescence signals (image B) and results in Raman map of bone locations.

The two images, each at different wavelength, hold sufficient information to localize the unique Raman signatures of bone by image subtraction. This composite image represents a 2D map of the bone locations. Tomographic approach implementation is required in order to resolve embedded bone structures in tissue beyond 5 mm depth, in order to resolve distance and size features. The adipose tissue and cortical bone selected for this experiment were taken from a food-grade bovine sample. No Institutional Review Board approval was required. 1 mm bone segments were chosen to represent the detection size limit (slice width) of medical x-ray (CT) systems. The x-ray scans were taken by a high-resolution microCT (SkyScan 1172, Bruker MicroCT N.V., Kontich, Belgium) at an image resolution of 27.4 µm (70 kV

#239577 Received 22 Apr 2015; revised 19 Jun 2015; accepted 29 Jun 2015; published 10 Sep 2015

and 141 μA radiation source, using a 0.5mm aluminum filter), and imaged using DataViewer software provided by the manufacturer.

3. Results

Our proof of concept macro-imaging Raman system is adapted to acquire full field images of tissue in real time without resolving Raman spectra, to capture the location of bone tissue structures (Fig. 3). By using the unique Raman stokes signature of the Phosphate (PO_4^{3-}), specifically the tetrahedral symmetric stretching of the P-O bonds [1–4], a successful detection of the inorganic constituent within the bone structure is possible. Phosphate is a major building block of hydroxyapatite, the calcium mineral found in bone and heterotopic ossification, and is not found in significant quantities in other tissues. This signal can overcome the broad fluorescence background found in bone and tissue, and ultimately can enable *in vivo* detection. The spectra and algorithm are depicted in the methods section (Fig. 2).

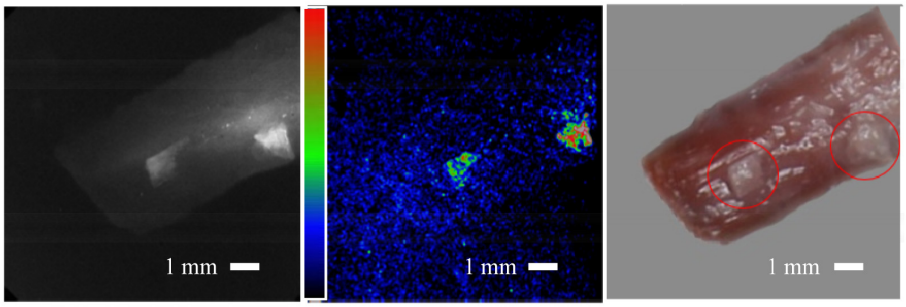

Fig. 3. Bone on tissue imaging. Right: Conventional color image taken after the experiment showing the tissue sample with 2 pieces of bone on top encircled in red, image rotated on grey background to match fluorescence and Raman images orientation. Adipose tissue and cortical bone fragments were taken from bovine samples. Left: Grey scale image of the fluorescence and Raman signals at optical wavelength of 852 nm (excitation wavelength is at 785 nm), showing both the bone and the soft tissue fluorescence signals. Middle: Raman signal computed image showing the bone locations. The muscle tissue fluorescence signal reduced significantly and showing close to background signal level. Bone signal is measured at about x10 larger than the surrounding tissue, which translate to 20 dB in Signal to Noise Ratio (SNR). Image threshold has been applied, due to laser beam non-uniformity signal levels from the two bone pieces at the two locations are different. Field of view in all images is 1 cm x 1 cm.

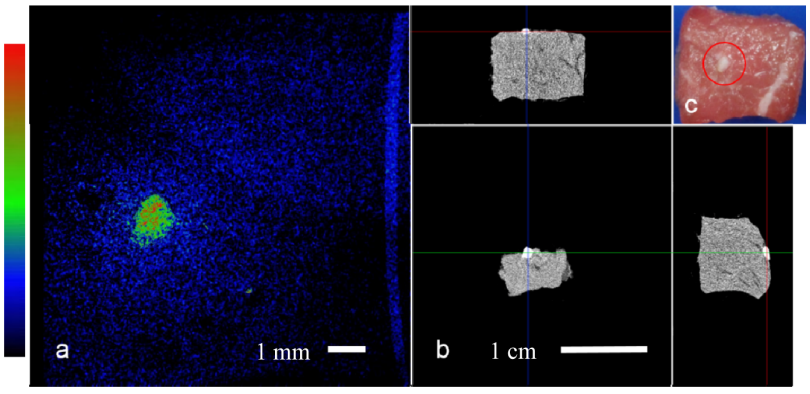

Fig. 4. Bone on tissue imaging: a. Top view Raman computed image of the tissue sample field of view is 1 cm. b. microCT projections of the sample, top and perpendicular side views. c. Top view color image with bone fragment encircled in red, bone size is ~1 mm.

#239577 Received 22 Apr 2015; revised 19 Jun 2015; accepted 29 Jun 2015; published 10 Sep 2015

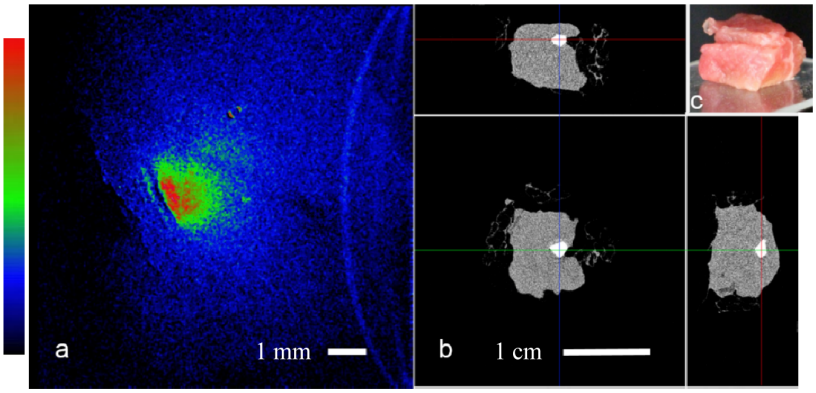

Fig. 5. Bone embedded in tissue: a. Raman computed image of the tissue sample, the bone (~1 mm in size) Raman signal scattered through the top layer showing diffused boundaries and effectively lowering resolution, field of view is 1 cm. b. microCT projections of the sample, top and perpendicular side views, scale bar 1 cm. c. Angled side view color image, showing top layer of meat (~2 - 3 mm thickness), and a bottom piece (~8 mm).

Further experiments conducted with collaboration of the dental school, enabled validation of the imaging results using a microCT scanner (Figs. 4 and 5). These preliminary experiments provide support for our imaging approach and show that we can detect a 1 mm bone fragment through 3 mm of bovine adipose tissue. The imaging result in Fig. 3 was acquired using the ICCD, with 2 seconds total acquisition time. The ICCD's built-in image intensifier enables fast imaging with high sensitivity, however, the resulting images exhibit lower effective resolution due to the amplification process. Results in Figs. 4 and 5 were taken using the NIR camera with acquisition time of 8 seconds. This camera acquired higher resolution images with longer exposure times due to lack of signal amplification. Both cameras achieve similar SNR (with different noise characteristics) and are capable in producing acceptable results. The preferred sensor will depend on specific imaging needs including; determination of the required imaging speed, ease of implementation, and cost. These considerations will be better defined in future research efforts.

4. Conclusion

The direct Raman detection system has potential to detect bone Raman signals *in vitro* with settings that comply with *in vivo* conditions both in illumination intensity and speed. Further experiments are required in order to find the detection limits with respect to bone size and depth. Using trabecular bone (spongy bone) samples with lower hydroxyapatite concentration is planned in order to better simulate HO conditions. This will require an increase in the illumination power that can enable larger illumination area and offer better beam uniformity. Variable illumination and acquisition orientation can also be implemented in a tomographic imaging routine in order to better localize in-depth bone tissue locations.

Acknowledgements

We thank Dr. Kang Ting for providing the microCT scans, Justine Tanjaya for experimental support, and Chris Campillo from Andor Technology for loaning the NIR camera. This work was sponsored by the DoD Telemedicine & Advanced Technology Research Center (TATRC), grant# W81XWH-12-2-0075.

#239577 Received 22 Apr 2015; revised 19 Jun 2015; accepted 29 Jun 2015; published 10 Sep 2015